Biotechnology Advances 31 (2013) 375–386

Contents lists available at SciVerse ScienceDirect

Biotechnology Advances

journal homepage: www.elsevier.com/locate/biotechadv

Imaging cells and sub-cellular structures with ultrahigh resolution full-field X-ray microscopy

C.C. Chien [a,b], P.Y. Tseng [a], H.H. Chen [a], T.E. Hua [a], S.T. Chen [a], Y.Y. Chen [a], W.H. Leng [a], C.H. Wang [a], Y. Hwu [a,b,c,d,*], G.C. Yin [e], K.S. Liang [f], F.R. Chen [b], Y.S. Chu [g], H.I. Yeh [h], Y.C. Yang [h], C.S. Yang [i], G.L. Zhang [j], J.H. Je [k], G. Margaritondo [l]

[a] Institute of Physics, Academia Sinica, Taipei 115, Taiwan
[b] Engineering and System Science, National Tsing Hua University, Hsinchu 300, Taiwan
[c] Institute of Optoelectronic Sciences, National Taiwan Ocean University, Keelung 202, Taiwan
[d] Advanced Optoelectronic Technology Center, National Cheng Kung University, Tainan 701, Taiwan
[e] National Synchrotron Radiation Research Center, Hsinchu 300, Taiwan
[f] Electrophysics Department, National Chiao Tung University, Hsinchu 300, Taiwan
[g] NSLS-II, Brookhaven National Laboratory, Upton, NY 11973-5000, USA
[h] Mackay Memorial Hospital, Taipei 104, Taiwan
[i] Center for Nanomedicine, National Health Research Institutes, Miaoli 350, Taiwan
[j] Shanghai Institute of Applied Physics, Chinese Academy of Sciences, Shanghai 201800, China
[k] X-ray Imaging Center, Pohang University of Science and Technology, Pohang 790-784, Republic of Korea
[l] Ecole Polytechnique Fédérale de Lausanne (EPFL), CH-1015 Lausanne, Switzerland

ARTICLE INFO

Available online 21 April 2012

Keywords:
X-ray microscopy
Phase contrast radiology
Fresnel phase zone plate
Subcellular organelle

ABSTRACT

Our experimental results demonstrate that full-field hard-X-ray microscopy is finally able to investigate the internal structure of cells in tissues. This result was made possible by three main factors: the use of a coherent (synchrotron) source of X-rays, the exploitation of contrast mechanisms based on the real part of the refractive index and the magnification provided by high-resolution Fresnel zone-plate objectives. We specifically obtained high-quality microradiographs of human and mouse cells with 29 nm Rayleigh spatial resolution and verified that tomographic reconstruction could be implemented with a final resolution level suitable for subcellular features. We also demonstrated that a phase retrieval method based on a wave propagation algorithm could yield good subcellular images starting from a series of defocused microradiographs. The concluding discussion compares cellular and subcellular hard-X-ray microradiology with other techniques and evaluates its potential impact on biomedical research.

1. Introduction

The development of new microscopy methods is a key element in the historical progress of biological and biomedical research. A landmark for each microscopy technique is the detection of individual cells and of their internal structure (Fischer et al., 2011; Marsh et al., 1971; Marton, 1941; Porter et al., 1945; Tanaka and Fukudome, 1991). For over one century, X-rays did play a fundamental role in biomedical research — but they were so far unable to image internal cell features in tissues. In a series of recent experiments, we achieved this important objective.

Our strategy was based on a combination of factors to improve the image contrast and spatial resolution. One of them was the use of highly bright and coherent X-rays emitted by synchrotron sources. The coherence specifically facilitated the task of focusing the radiation to improve the resolution. Furthermore, it enabled us to improve the image contrast by exploiting mechanisms (Cloetens et al., 2002; Hwu et al., 2002) based on the real part of the refractive index rather than on absorption (the imaginary part). These mechanisms – conventionally called "phase contrast radiology" – strongly enhance the contrast between soft tissues in biological specimens.

Our experiments used short-wavelength (~1 Å) X-rays capable to penetrate thick specimens in a natural state. On the contrary, previous microradiology tests were based on long-wavelength soft-X-rays in the "water window" (23–45 Å) that maximize the contrast between carbon-containing areas and water (Jacobsen et al., 2002; Kirz et al., 1994). With advanced soft-X-ray optics, subcellular structures could be observed in hydrated states (Larabell and Nugent, 2010; McDermott et al., 2009). However, soft-X-rays cannot penetrate specimens thicker than a few cells (≈10 μm) and are thus unsuitable for cell studies at the tissue level. This is a rather severe

* Corresponding author at: Institute of Physics, Academia Sinica, Taipei 115, Taiwan. Fax: +886 2 2789 6721.
E-mail address: phhwu@sinica.edu.tw (Y. Hwu).

0734-9750/$ – see front matter © 2012 Elsevier Inc. All rights reserved.
doi:10.1016/j.biotechadv.2012.04.005

limitation (similar to visible light microscopy) that largely offsets the advantages of the high spatial resolution.

In a precursor experiment, we used hard-X-rays to image individual cells in a fresh and unstained state (Hwu et al., 2004) — the probed tissue thickness reaching several mm. Such tests included time-resolved experiments and tomographic reconstruction. However, they did not yet produce high-quality images with subcellular resolution.

We could finally reach this key objective by magnifying the X-ray images with Fresnel zone-plate objectives fabricated with state-of-the-art nanotechnology (Chu et al., 2008; Lo et al., 2007a, 2007b). These devices yielded a spatial (Rayleigh) resolution down to <20 nm (Chen et al., 2011a) and an image acquisition time below 50 ms (Chen et al., 2008a, 2008b).

We used staining to label and detect specific targets while locating proteins inside the cells and investigating sub-cellular organelles. This required a specific effort to develop suitable staining procedures since those used for other techniques, such as visible, confocal and fluorescence microscopies, do not fully match the needs of hard-X-ray microscopy. Specifically, staining methods for emission microscopy are not relevant to absorption or phase contrast X-ray images. Our staining/labeling method, based on immunocytochemistry, widely used for TEM (transmission electron microscopy), enabled us to investigate with nanometer resolution specific protein structures and distributions in two and three dimensions (3D). However, modifications of the staining materials and procedures were required because of the large difference in the specimen thickness for TEM and X-ray microscopy. Indeed, most of the heavy metal staining used for TEM is for thin (<1 μm) sections, and does not guarantee uniformity on our >100 μm specimens. We thus adopted and extended exposure to the staining solution.

Compared to previous soft-X-ray microscopy approaches, our method offers marked advantages. It penetrates much deeper into the specimen: intracellular details within >5 mm thick specimens could be clearly identified without critically decreasing the spatial resolution. As to hard-X-rays, previous tests (Hsieh et al., 2004; Jiang et al., 2010) could reach nanoscale resolution only by applying sophisticated phase retrieval methods to diffraction imaging. Recent developments in coherent diffraction imaging significantly simplified the image reconstruction; however, we reached subcellular resolution with no image processing. However, we did explore the use of a phase retrieval technique based on a wave propagation algorithm (Barty et al., 2000; Hsieh et al., 2004; Yin et al., 2007) to reduce or eliminate the need for staining. This approach yielded separate phase and amplitude images at the subcellular level.

As to possible future improvements, efforts are underway to achieve more versatile functional labeling and functional imaging on the nanometer scale. The current <30 nm lateral resolution of our zone plate objective is far from the theoretical diffraction limit and also from the estimated instrumentation limits. With even better zone-plate nanofabrication the lateral resolution – primarily determined by the smallest outer zone – can be further enhanced: outer zones ~20 nm were already achieved (Chen et al., 2008b, 2011b; Chu et al., 2008; Lo et al., 2007a, 2007b) yielding resolutions <20 nm. New high brightness X-ray sources will likely decrease the exposure time reducing for example the motion blur for live specimens. Furthermore, they would enable us to use higher-order diffraction modes (Yi et al., 2011; Yun et al., 1999) of the zone plates and further enhance the lateral resolution — although with a decreased signal and therefore a longer image acquisition time.

2. Materials and methods

2.1. Instrumentation

The experiments were performed on the beamlines 01A and 01B of the National Synchrotron Radiation Research Center (NSRRC) in Taiwan (Song et al., 2007), the 32-ID-D beamline of the Advanced Photon Source (APS, Argonne) (Shen et al., 2007) and the 7B2 beamline of the Pohang Light Source (PLS) (Baik et al., 2004). Specifically, tests with high spatial resolution were implemented on the NSRRC 01B and APS 32-ID-D beamline whereas the two other facilities were used for experiments with more limited resolution but faster image taking.

The high-resolution NSRRC and APS facilities are equipped with ultrahigh resolution transmission X-ray microscopes (TXM) including custom-designed microimaging systems with *ad hoc* fabricated Fresnel zone-plates (Chen et al., 2008b; Chu et al., 2008). The X-ray source is a 5-T superconducting wavelength shifter (SWLS) inserted along the 1.5 GeV NSRRC ring and an undulator at the 7 GeV APS ring.

The X-rays generated by these insertion devices are monochromatized by double crystal monochromators and then focused into the specimen by condenser lenses. The transmitted radiation is processed by the zone plate magnifying objective and projected into an array detector — consisting of a CCD camera with a 20× optical objective lens coupled to a scintillator. The total magnification of the zone-plate plus the visible light imaging system is 900–2400×.

The gold zone plates used for the present experiments were fabricated on thin (100 nm) SiN_x membranes and have ~1.5–3 cm focal length, a diameter of 85 μm, thickness up to >450 nm (corresponding to aspect ratios in excess of 15) and a 30 nm outermost zone width. To obtain phase contrast for low X-ray absorption materials, the microscopes are equipped with Zernike gold phase rings. The selected photon energy of 8 keV simultaneously optimizes the zone plate effectiveness and the contrast. The typical exposure time for a single image with 900× magnification is ~50 ms.

We used zone plates with 25 nm outermost zone width as the best compromise between efficiency and spatial resolution for this particular study. We measured the spatial resolution with the Rayleigh criterion (for the procedure, see Chu et al., 2008), using a standard test pattern whose smallest feature size was ~30 nm. Images such as those in Supporting Information Fig. SI1 confirmed that the smallest features are visible, corroborating the resolution measurements. The resolution measurements were performed both before and after the experiments.

Details about the two other experimental facilities, 01A at NSRRC and 7B2 at PLS, can be found in refs. Baik et al. (2004) and Song et al. (2007). The main difference with respect to the ultrahigh-resolution systems is that they use unmonochromatized X-rays, reaching more limited spatial resolution but gaining more than 3 orders of magnitude in time resolution compared to experiments with monochromatized X-rays. This is due to the fact that zone plates cannot be used with unmonochromatized X-rays: without zone plate magnification, the transmitted X-rays are directly detected by a cleaved $CdWO_4$ single-crystal scintillator and converted to visible images. These images are then magnified by an optical lens and captured and stored by a CCD camera. The resulting image taking is quite fast: for biological specimens with low X-ray absorption, a single image (typically 1600×1200 pixel, horizontal field of view (FOV) = 500 μm) can be obtained in 1 ms or less.

The specimens in both facilities are mounted on translation/rotation stages for precise positioning. The specimen can thus be moved along the X-ray beam direction, varying the specimen-detector distance from <1 mm to 1.2 m. This is specifically required for the phase retrieval method: a series of defocused images must indeed be taken at different specimen-detector distances. A similar method in the monochromatized facilities achieves phase retrieval in TXM.

2.2. Cell culture and staining

HeLa cells were cultured in Dulbecco's modified Eagle's medium (DMEM) supplemented with 10% calf fetal serum culture medium. EMT cells were cultured in Dulbecco's modified Eagle's medium and

F12 medium (DMEM–F12) supplemented with 10% calf fetal serum culture medium.

For vimentin staining, HeLa cells were fixed by 4% paraformaldehyde, blocked by 3% bovine serum album (BSA) in phosphate-buffered saline (PBS) plus 0.1% Triton-X 100 to eliminate the non-specific binding and by 0.1% H_2O_2 to neutralize the endogenous peroxidase. We are specifically targeting vimentin, an intermediate filament protein (58 kDa) found in a variety of cells of mesenchymal origin that helps in supporting cellular membranes, nuclei, and other intracellular organelles. To localize the vimentin inside the cytoplasm, cells were then incubated in 100× diluted primary antibody vimentin (from Dako®) for 2 h at room temperature.

For tubilin staining, EMT-6 cells were fixed and stained with the monoclonal anti-α-tubulin clone B-5-1-2 purified mouse immunoglobulin (mouse IgG1 isotype) (T6074, Sigma) diluted 1:5000 in BSA-containing PBS buffer at room temperature for 1 h. Secondary staining was performed with peroxidase conjugated goat anti-mouse IgG antibody diluted 1:1000 in BSA-containing PBS buffer at room temperature for 1 h.

After rinsing with PBS, the cells were further incubated in 200× diluted secondary antibody with peroxidase conjugation (Chemicon®) for 1 h. DAB (3,3′-diaminobentidin) substrate kit was applied for 4–6 h to obtain gray and black cells. DAB with nickel enhancement kit was from VectorLab® (SK-4100, Vector Laboratories, Inc.). For immunogold vimentin labeling, HeLa cells were incubated with FluroNanoGold-conjugated secondary antibody (Nanoprobes®) for 1 h and then with silver enhancement kit (Nanoprobes®) for 20 min. After staining, cells were dehydrated in series of ethanol and then air dried. In addition to the X-ray imaging tests, experiments were performed with confocal fluorescence laser imaging; the corresponding specimens were obtained by incubation with a Cy3 fluorophore conjugated secondary antibody.

2.3. Tumor tissue specimen

For tissue studies, EMT-6 cells were subcutaneously inoculated into the thigh of the Balb/C mouse. During the next 8 days, the tumor size grew to 50–90 mm^3. The mice were then injected with 100 μl of 75 mg/ml PEG-Au gold nanoparticles and sacrificed after 24 h. Tumor tissue was removed and then fixed by immersion in 3.7% formaldehyde in phosphate buffered saline (PBS). The tumor tissue was stained with osmium for 2 h. After staining, these samples were hydrated by a series of differently diluted ethanol solutions and embedded in resin. The specimens were finally cut into 100–200 μm pieces.

2.4. Plant tissue preparation

The skin of the graptopelaum paraguayense was cut into small pieces before being prepared by either high presure cryogenic fixation and water substitution or standard electron microscopy staining followed by a dehydration process. For cryofixation, samples were stored in a high pressure cryofixation machine (Leica EM PACT2) at −90 °C for 20 min and then transfered to freeze-substitution system (Leica EM AFS2) in 100% ethanol, at −90 °C. After that, samples were stained with uranyl acetate 0.5% for 1.5 h and then washed with ethanol. After 3 days, ethanol temperature was increased to −60 °C, then changed with new 100% ethanol for 18 h. Finally, sample ethanol temperature was further increased to −20 °C and changed with new 100% ethanol for 8 h before embedded in LR Gold™ resin.

Another sample is directly fixed with 2.5% glutaraldehyde/4% para-formaldehyde overnight, then post fixed with osmium tetroxide 1% for 12 h. After that, samples were stained with uranyl acetate 0.5% 1.5 h and then dehydrated in series ethanol and the samples were dried in air.

2.5. Zebrafish staining

Experiments were also performed on other bio-systems. For large-scale tissue imaging tests, five-day-old zebra fish specimens were stained using the Golgi method, fixed with 4% para-formaldehyde overnight and then mounted in 2.5% potassium dichromate in the dark. After three days, they were transferred into 0.1 M silver nitrate and left there in the dark for three 3 additional days. After sequential dehydration by 30%, 50%, 70%, 95%, 100% gradient ethanol and acetone, the specimens were embedded in an epoxy resin (Sigma®).

2.6. Mouse aorta specimens preparation

Mouse aorta specimens were prepared with the following procedure. Adult C57/BL6 mice were anesthetized with ether inhalation and perfusion-fixed *via* direct intracardiac injection, with heparinized PBS (10 units/ml) followed by phosphate-buffered 2% paraformaldehyde (pH 7.4) for 10 min (Blackburn et al., 1995). The thoracic aortae were dissected obtaining transverse rings. Such rings were embedded in the resin using standard preparation procedures for thin-section electron microscopy (Blackburn et al., 1995; Yeh et al., 2003).

3. Results

3.1. High-resolution experiments at the subcellular level

Fig. 1 illustrates the progress from imaging tests with unmonochromatized X-rays to high-resolution hard-X-ray microscopy. Thanks to the DAB staining with nickel enhancement, the vimentin network of the HeLa cells can already be seen in the phase-contrast image of Fig. 1A, obtained with unmonochromatized X-rays. The spatial resolution (~1 μm) is similar in this case to optical microscopy. We can clearly observe stained vimentin and nuclei within the cells (FOV = 240 μm). The nucleus is not affected by the staining procedure and therefore has weak X-ray absorption. The cytoplasm appears darker than the nucleus since it contains dense stained vimentin especially in the peri-nucleus area that produces X-ray absorption, as confirmed by optical microscopy.

Fig. 1B demonstrates that hard-X-ray microscopy with zone-plate magnification surpasses the diffraction limit of optical microscopy without using nonlinear or stochastic properties of fluorophores (Rittweger et al., 2009; Wang et al., 2011a). Indeed, it shows that for specimens like Fig. 1C the texture of vimentin bundles near the nucleus can be clearly identified. Vimentin also appears as a meshwork structure in the peri-nucleus area; the nucleus and the cell boundaries are thus visibly delineated. Besides the vimentin bundles, single filaments are also observed.

Similar test on a different type of cell, EMT-6 with tubulin staining clearly shows the 3D structure of the cytoskeleton. In Fig. 2C, we see tomography images reconstructed from the area shown in Fig. 2A.

Fig. 3 shows a high-resolution hard-X-ray microscopy image for HeLa cells stained with FluroNanoGold with silver enhancement: individual vimentin bundles are observed in the cell filopodia (indicated by arrows). The aggregated FluroNanoGold can also be detected inside the cells as marked by circles. The smallest detectable vimentin bundles are <100 nm wide, proving that the actual resolution is close to the measured 60 nm resolution level of the zone-plate used for this particular experiment.

The detection of individual nanoparticles is only possible with sufficient resolution. When this requirement is met, single nanoparticles can replace staining. Fig. 4 shows a high resolution X-ray micrograph and tomography reconstructed images (see also movie SI4D in Supplementary Data) of EMT-6 cells co-cultured with Au nanoparticles, revealing the uptake of Au nanoparticles and the accumulation

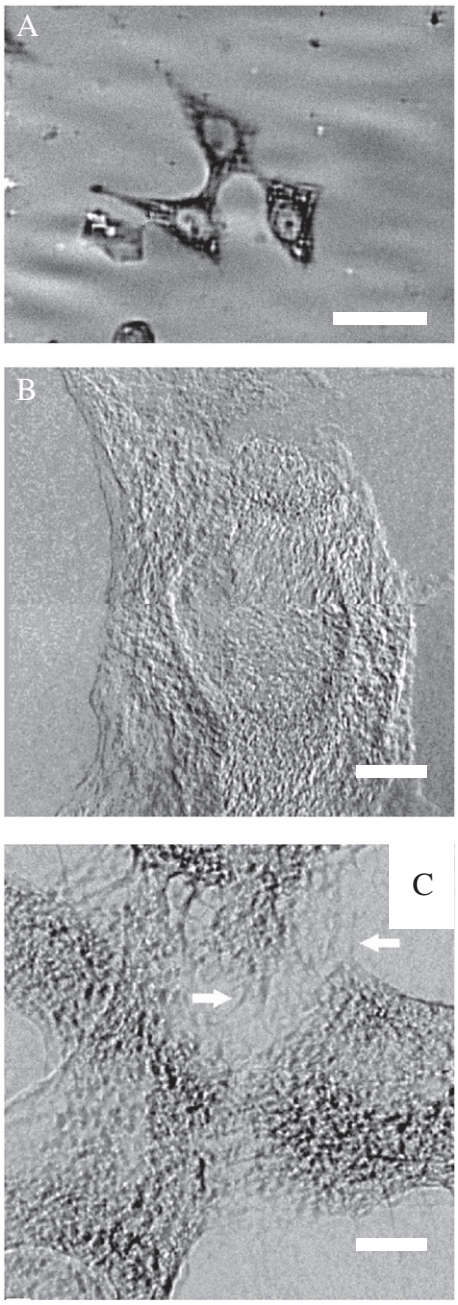

Fig. 1. Micrographs of HeLa cells showing a vimentin network stained by DAB with nickel enhancement. A: X-ray micrograph obtained with unmonochromatized synchrotron X-rays, bar = 50 μm. B: patchwork of 4 microradiographs of the same specimen taken with a zone plate X-ray microscope that yields much better resolution and image quality. Specifically, the vimentin inside the cell and outside the nucleus is visible as linear arrays throughout the cytoplasm. C: the texture of vimentin bundles close to the nucleus can be clearly identified. Bar = 5 μm (B, C).

near cell nuclei (Chen et al., 2011c). The cells are not stained but the nucleus is clearly outlined by the Au nanoparticles. This approach could eventually be applied for the detection of specific molecules using the immune-gold labeling methods of TEM. Preliminary steps in that direction were recently achieved with different Au nanoparticle systems which specifically bind to certain proteins (Lai et al., 2011).

The ability to detect nanoparticles is particularly important for imaging at the tissue level. Au nanoparticles can be clearly detected in tissues obtained from organs such as the liver, kidneys and spleen after they are injected *via* the tail vein. Fig. 5 shows a

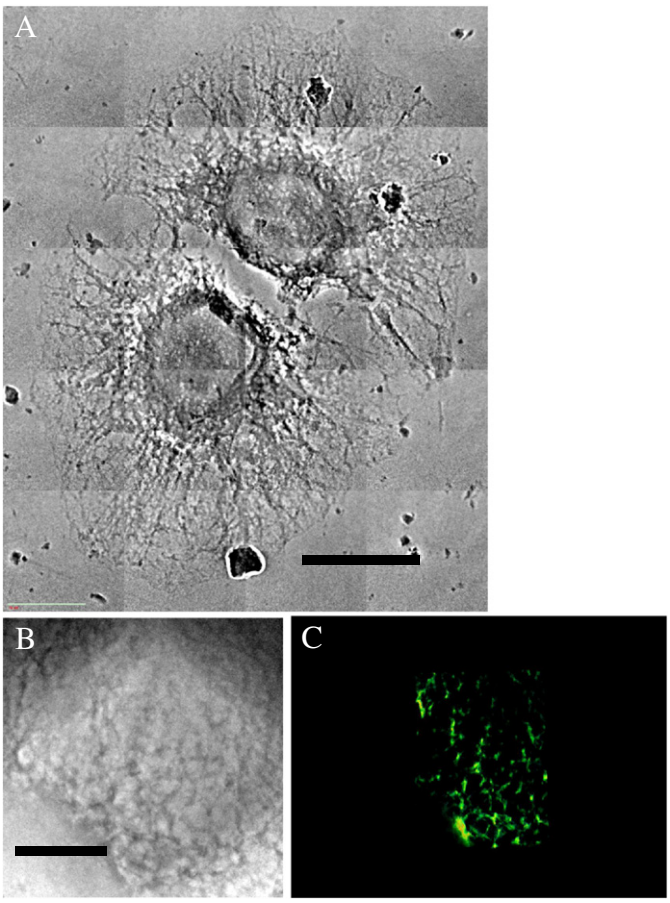

Fig. 2. Tests similar to Fig. 1, conducted on a different type of cell, EMT-6 with immunostaining against tubulin. The image clearly shows the 3D structure of the cytoskeleton. C: one view of panel B tomography images reconstructed from the area shown in (B). Bars: 15 μm (A) and 5 μm (B).

tumor thick tissue where PEG-Au nanoparticles are localized on the cell membranes. This type of imaging approach can substantially shorten the specimen preparation time compared to other methods such as TEM — and can give much more precise and quantitative uptake estimations. Our tests also detected other subcellular organelles besides the cytoskeletons. By using a variety of staining methods, we specifically imaged actins, mitochondria and Golgi complexes.

3.2. High-speed microradiology of living cells

Time resolution is an interesting feature that enables X-ray microscopy to study evolving biological systems. Fast image taking is specifically important when observing cells in their natural environment, since their movements can blur the images and degrade spatial resolution. We would like, therefore, to assess the present situation as far as time resolution is concerned.

We have seen that the image-taking time for our highest spatial resolution (with zone-plate magnification) is of several tenths of seconds; this is longer than many relevant time scales for physiological functions. Therefore, a compromise is often required between spatial resolution and time resolution. In our tests, we obtained millisecond-resolution images – suitable for real-time bio-experiments – when using unmonochromatized X-rays and no zone plate magnification. To the best of our knowledge, no other technique can reach this combination of performances.

Interesting real-time results were obtained for plant cells — for which the lateral resolution without a zone plate is already sufficient

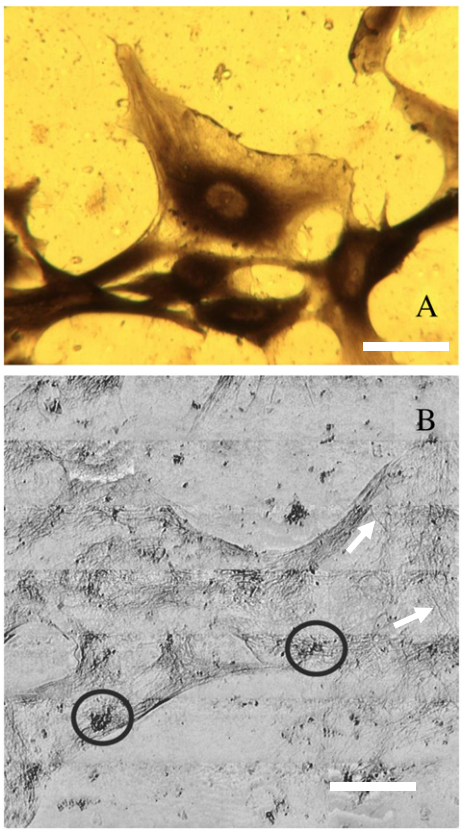

Fig. 3. Immunogold labeled the cytoskeleton of vimentin in HeLa cells. A: optical image of the cell similar to Fig. 1B using a different staining method: immunogold labeled vimentin (FluroNanoGold with silver enhancement). Bar: 25 μm. B: high resolution X-ray micrograph shows the stained vimentin at the cell margins and individual vimentin bundles in the cell filopodia (such as those indicated by arrows). This image was taken with a (Zernike) phase ring producing enhanced phase effect. The picture is a patchwork of 7×7 smaller images. The locations of aggregated Au nanoparticles are marked by circles. Bar: 20 μm.

to observe subcellular features. Fig. 6, for example, shows the opening–closing movement of stoma cells (Hwu et al., 2004). The live detection of such minute movements is quite remarkable if one considers the complete absence of staining for these specimens. Recently, positive results were also obtained for living yeast cells.

3.3. Tomographic reconstructions

Fast image-taking is also important for high resolution tomographic image processing that requires thousands of raw (projection) pictures. Once again, a reasonable compromise must be sought between the spatial resolution and the time resolution.

Fig. 7 shows tomography results with high spatial resolution for vimentin bundles near a nucleus in a HeLa cell specimen similar to Figs. 1 and 3. We specifically see in Fig. 7A a patchwork of nine projection images showing several overlapping cells: the 3D distribution of vimentin bundles near the nucleus is clearly visible. Fig. 7B and C shows projection images of the cell nucleus taken at different angles separated by 7° (see also the movie SI7B in Supplementary Data).

Fig. 7D shows a volume-rendered tomographic reconstruction of the nucleus of a HeLa cell based on a set of 90 images like Fig. 7B and C (see also movie SI7D in Supplementary Data). Even with this limited-angle local tomography procedure, the reconstruction process does not result in a major deterioration of the spatial resolution. Thus, high resolution tomographic reconstructions of subcellular features are demonstrated.

The major limiting factor in tomography is the accuracy of the sample position during rotation. With our setup, the accuracy is sufficient to achieve a micron-level spatial resolution in the reconstructed tomography images. For better resolution, projection images must be realigned using a sharp feature in the images as reference for alignment before tomography reconstruction. The sharp feature cannot be reliably identified at present by computer processing and is manually executed. This is a time-consuming process that limits the total number of projection images that can be processed and used for reconstruction. Furthermore, suitable reference features are sometimes difficult to find in bio-specimens. Tomographic procedures in general are easier with unmonochromatized X-rays and no zone plate magnification since thousands of projection pictures can be taken in a few seconds.

Fig. 8 shows the tomographic reconstruction (see also movie SI8A and SI8B in Supplementary Data) (by a standard filtered back-projection algorithm) of the ~2 mm thick, freshly prepared skin of an aloe leaf around a stoma. The image acquisition for each of the 360 projection images was 10 ms. Results like those of Fig. 8 demonstrate that the reconstruction does not significantly affect the resolution. Specifically, we observe only limited blurring by "local tomography" effects (Anastasio et al., 2003; Faridani et al., 1997) due to the fact that the specimen is larger than the FOV of each projection.

Fig. 9 shows an advanced example of tomographic reconstruction with high spatial resolution. The specimen is the same as for Fig. 5: a thigh tumor with Au nanoparticles. Three different reconstructed images are shown, revealing the so-called EPR (enhanced permeation and retention) effect: Au nanoparticles (the orange features) preferentially accumulate in tumors (Chien et al., 2010; Liu et al., 2008, 2010; Wang et al., 2007, 2008, 2011b).

3.4. Radiation damage

High-speed imaging makes it possible to obtain results before the radiation can noticeably damage the specimen. This issue was tested in a previous work (Hwu et al., 2004) on cultured and fixed neuron cells from a mouse brain as well as on animal cells in their wet states. The corresponding results are corroborated by the present experiments. In essence, we did not find detectable radiation damage during image acquisition for any of the cases discussed here.

This encouraging conclusion is not entirely surprising since the effectiveness of phase contrast limits the exposures and the consequent radiation effects. However, the possibility of radiation damage cannot be automatically neglected — and the issue must still be fully explored, in particular for tomographic processes using a large number of projection images.

To achieve even higher spatial resolution with zone-plate magnification, longer exposure times would be required and could possibly lead to detectable radiation effects. The photon flux at the sample position for both white light imaging and TXM is typically 1×10^{12} photon/s/mm^2. In the case of TXM, the capillary condenser intercepts only ~10% of the photon beam and produces a ~10 μm spot on the specimen. This is equivalent to a very high flux, $\sim1\times10^{21}$ photon/s/mm^2 which is likely to cause damage to biology specimens. Indeed, we observe bubbles and specimen distortion with ~1 s of exposure. Therefore, we cannot at this time obtain nanometer resolution for natural (wet) specimens, and we need specimen fixation for tomography. Fortunately, there still exists a large margin for improvements: for example, the current exposure time per frame (50 ms) and the corresponding dose could be reduced by 1–2 orders of magnitude with better detectors (Bech et al., 2008; Meyer-Ilse et al., 2001). A better efficiency of the zone plates could also decrease the dose, although probably to a smaller extent. Cryo-preservation could also become important (McDermott et al., 2009; Meyer-Ilse et al., 2001), and in general better specimen

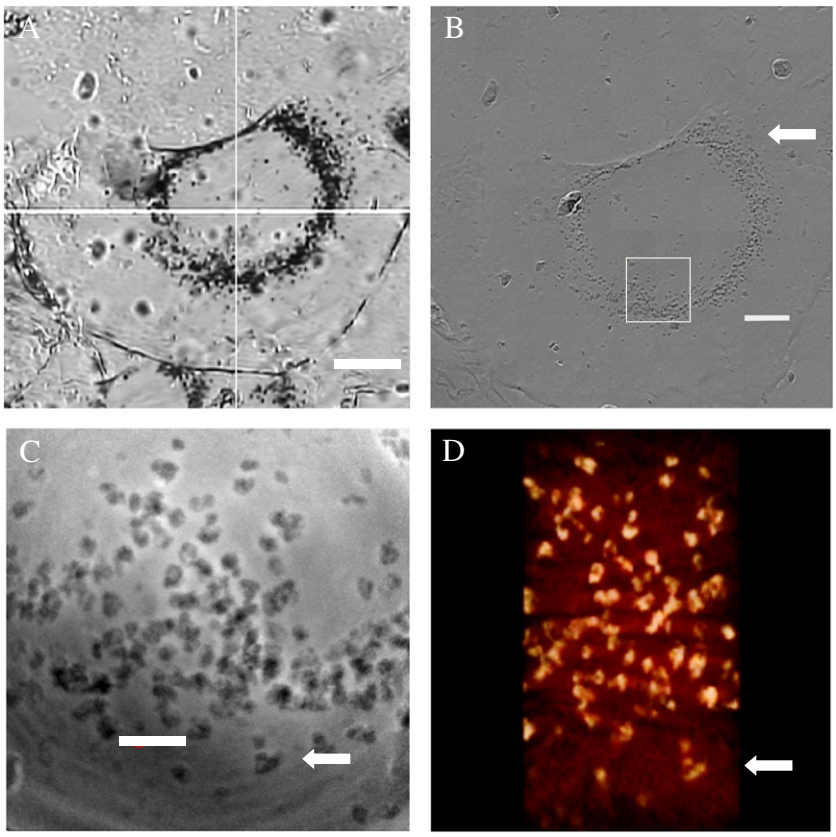

Fig. 4. High resolution X-ray micrograph of an EMT-6 cell co-cultured with Au nanoparticles (colloidal concentration 1 mM, culture time 24 h), showing Au nanoparticles accumulated near the cell nucleus. A: optical micrograph, B: patch work of 7×7 high resolution X-ray micrographs such as C. D: one view of the tomography reconstructed images (see also movie SI4D in Supplementary Data) of the sample area as (C). Bars: 20 μm (A); 15 μm (B); 2 μm (C).

preservation during the measurement could be required together with better specimen preparation: such measures are currently being investigated.

Fig. 10 shows the improvement of one of such specimen preparation strategy. The morphology of two specimens showed clear difference. Using the guard cells of the graptopelaum paraguayense again as an example, the high pressure cyrogenic fixation coupled with water substitution was able to fix and well preserve the fine structure of the cells (Fig. 10A) during the high resolution X-ray microscopy measurement with much reduced damage than that using

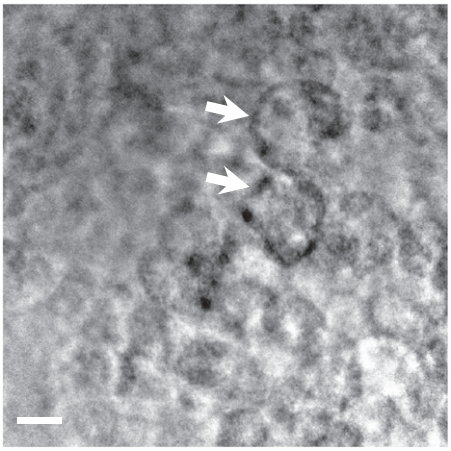

Fig. 5. Micrograph a 200 μm thick tissue specimen from a tumor-implanted mouse thigh after Au nanoparticle inoculation. Note that Au nanoparticles, marked by arrows, are localized on the cell membranes. Bar: 20 μm.

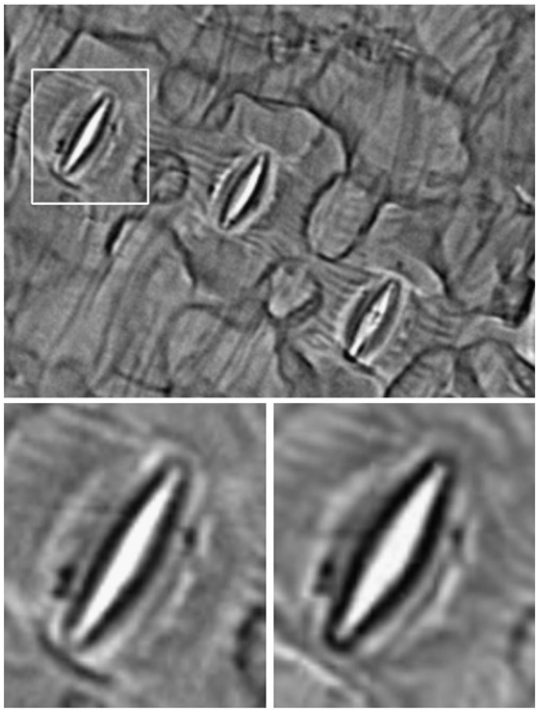

Fig. 6. Time-resolved microradiography of living cells. Top: microradiograph (0.35×0.47 mm^2) of a hippeastrum leaf taken with unmonochromatized X-rays and showing the leaf skin membrane. Bottom: two magnified images of the marked area on the top figure, revealing the opening–closing motion of a stoma cell. Note that the image was obtained without any staining.

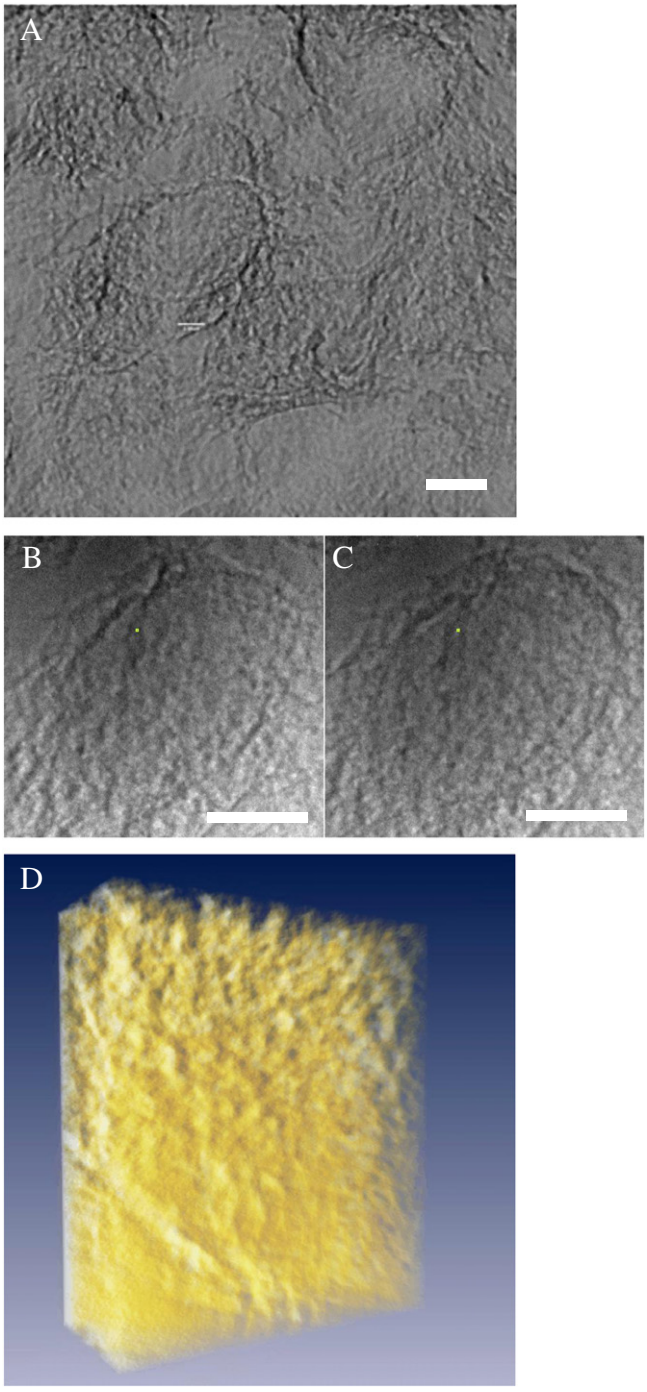

Fig. 7. High-resolution hard-X-ray tomography with limited angle reconstruction of a specimen of the same HeLa cells as in Figs. 1–2. A: patchwork of 9 projection images; bar = 5 μm. B, C: projection images (bar = 5 μm) showing one cell nucleus taken at different angles 7° apart from each other; D: volume-rendered solid model of the nucleus of one of the HeLa cells obtained by limited-angle local tomography reconstruction (see also movie SI7B and SI7D in Supplementary Data).

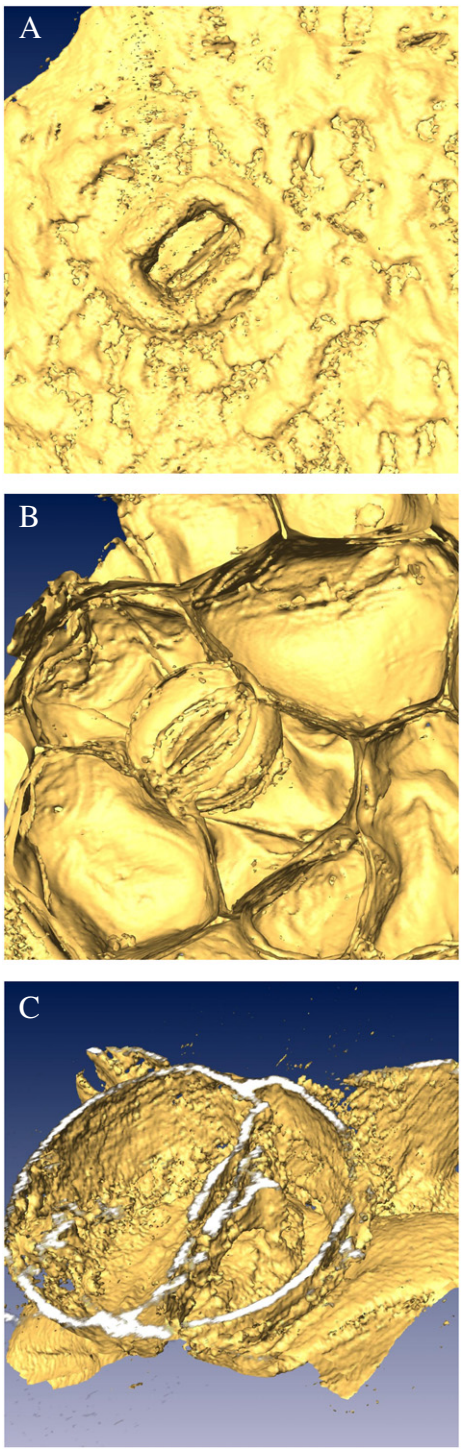

Fig. 8. Isosurface presentation of the tomographically reconstructed model of aloe leaf cells with a stoma. As in Fig. 6, the specimen was an ~5 mm thick freshly prepared hippeastrum leaf skin. The image-taking time was quite short: 10 ms per projection using the "local tomography" mode. A, B and C: "virtual slices" through the stoma revealing the cell structure in detail (see also movie SI8A and SI8B in Supplementary Data). The FOV: 250 μm (A, B) and 80 μm (C).

the normal dehydration method (Fig. 10B). Normal dehydration method specimen showed distorted and shrinkage.

3.5. Phase retrieval and contrast enhancement

Phase contrast is certainly helpful when absorption contrast is too limited. Beyond mere phase contrast, the retrieval of phases from the data could be interesting. The extreme case is the separation of phase and absorption effects in DEI (diffraction enhanced imaging).

We specifically explored the use of numerical phase retrieval methods. One of the most popular algorithms is the transport intensity equation (TIE) (Barty et al., 1998) that makes use of the relation between the phase and the intensity gradient. This non-interferometric procedure was exploited for phase retrieval in optical microscopy with partially coherent illumination (Bachim and Gaylord, 2003) and in X-ray microscopy using plane polychromatic

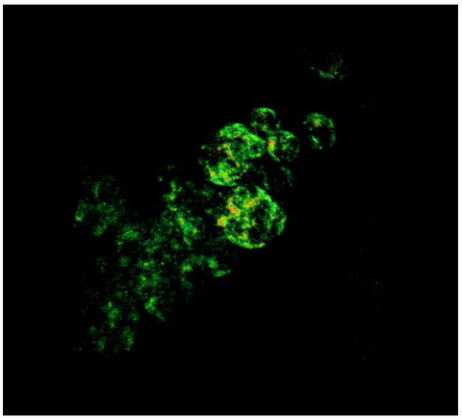

Fig. 9. Tomographic reconstructions with high spatial resolution of the same specimen as in Fig. 5. The orange features reveal the location of Au nanoparticles. FOV: ~200 μm.

waves (Paganin and Nugent, 1998). Iterative phase retrieval methods based on wave propagation were applied to phase recovery for soft X-rays (Allen et al., 2004b) and to obtain the exit wave in high-resolution TEM (Allen et al., 2004a; Hsieh et al., 2004). Both the smooth phase variations and the sharp object edges can be obtained with the propagation algorithm (Allen et al., 2004a; Hsieh et al., 2004).

We tested iterative phase retrieval for microradiographs taken both with the high-speed NSRRC 01A experimental system and with the NanoXCT system with Zernick phase rings (NCCR 01B). We present here results obtained with the wave self-consistent propagation algorithm (Hsieh et al., 2004) to retrieve the phase of the exit wave for partially coherent unmonochromatized synchrotron X-rays. The basic procedure involving a self-propagation algorithm for exit wave reconstruction can be summarized as follows:

(1) The phases of a through focal series of images (in which the number of images, N is greater than or equal to 3) recorded with different focal distances are set to zero to constitute the initial solutions.
(2) The exit wave is propagated to each image plane. The propagation of the wave to different image planes can be evaluated by multiplying a propagator in reciprocal space and then inverse Fourier transforming back to real space. The cross-correlation coefficient between the modulus of the propagated wave and the square root of the image intensity is calculated around the pre-determined focus value.
(3) The modulus of the propagated wave is replaced with the square root intensity of the experimental image at the focal plane giving a maximum in the cross-correlation coefficient, while the phase of the propagated wave is retained. This procedure also provides a refinement of the focus value and of the phase of the image wave.

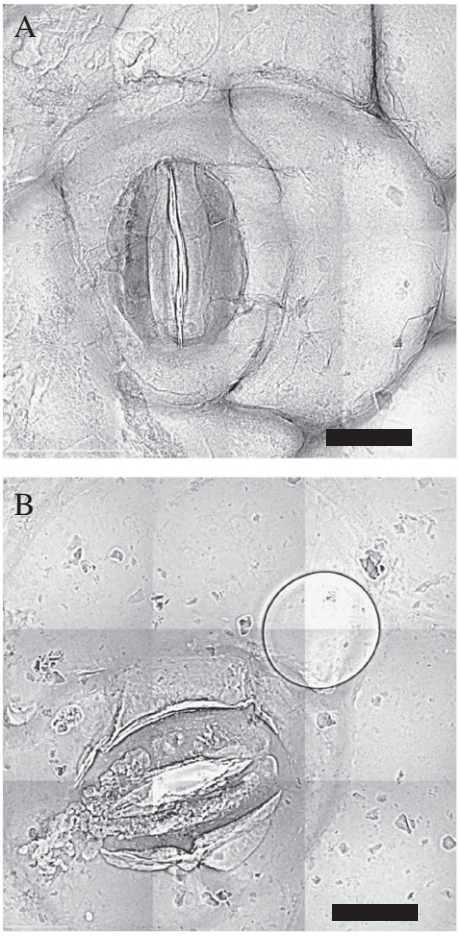

Fig. 10. High resolution X-ray micrographs of guard cells of graptopelaum paraguayense prepared with high presure cyrogenic and water substitution fixation method (A) and standard dehydration method (B). Note that the many bubbles in (B) are artifacts as a result of radiation damage, guard cell morphology changed and shrink. Bars: 10 μm.

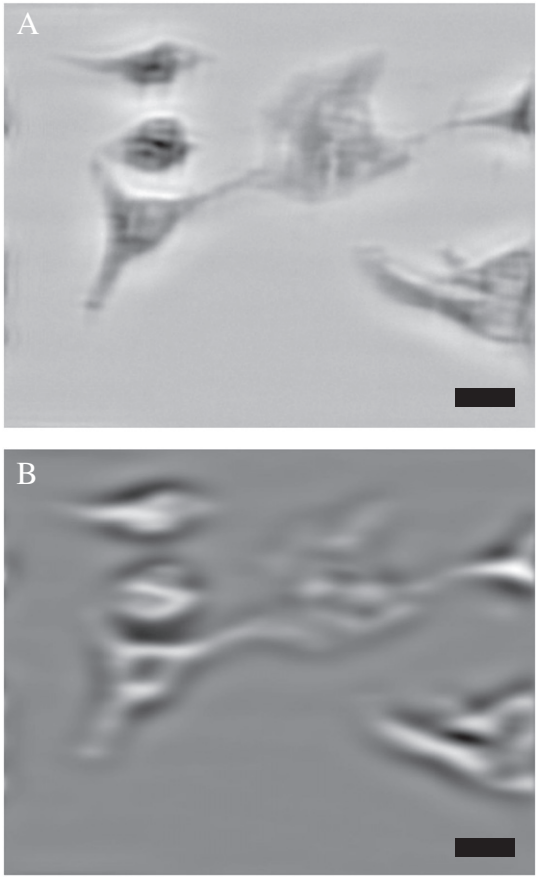

Fig. 11. Microradiographs of HeLa cells processed with the wave propagation algorithm. A: the amplitude map of the wavefront. B: the phase map. The comparison of the two images shows the effective separation of absorption and phase effects down to the sub-cellular level. Bar = 20 μm.

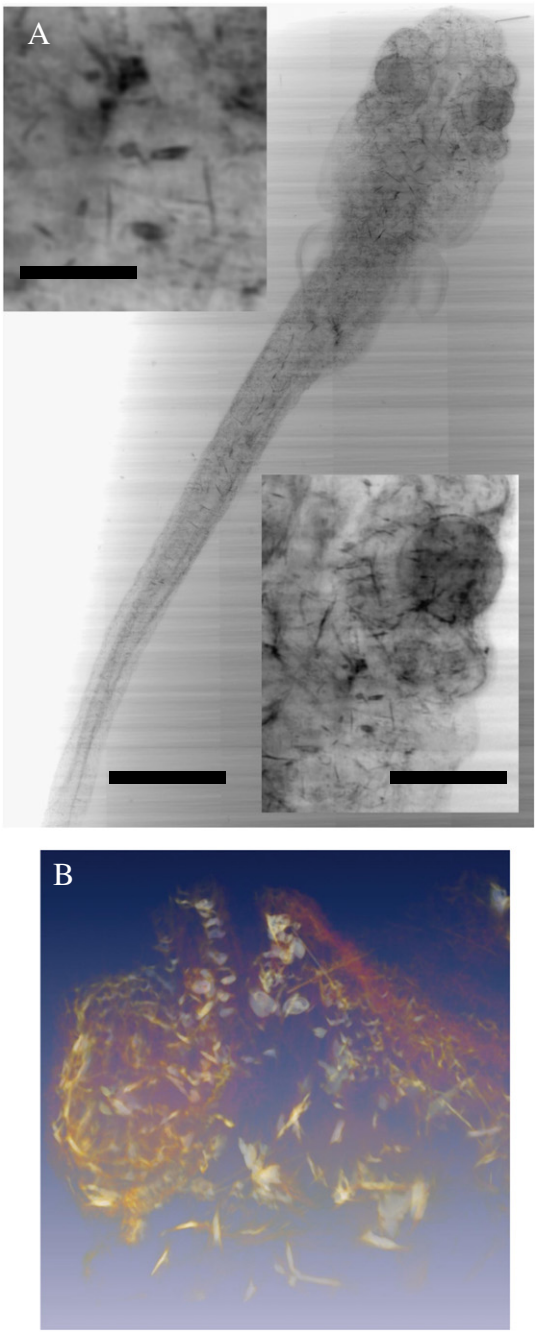

Fig. 12. An example of microradiology of thick specimens. A: microradiographs of the head of a zebra fish stained with the Golgi method. The arrows indicate individual cells revealed by staining. Bars: 500 μm and 100 μm (insets). B: volume rendered tomographic reconstruction: the bright spots indicate individual cells (see also movie SI12B in Supplementary Data). FOV: ~500 × 500 μm^2.

(4) Step (2) is repeated and the exit wave is re-calculated. Steps (2) and (3) are then iterated until a satisfactory figure of merit is reached.

In practice, the above approach was implemented in the MacTempas package (Margaritondo, 2002). We tested it for HeLa cells whose vimentin was stained by DAB with nickel enhancement to obtain a clear difference between the final amplitude and phase images. The experimental starting point was a set of images taken at 25 different sample-detector distances from 1 to 300 mm. The phase retrieval results – amplitude and phase images – are shown in Fig. 11.

In the amplitude image (Fig. 11A), the stained subcellular structure is clearly visible. In addition, subcellular structure not directly related to staining is visible in the phase image (Fig. 11B). This indicates that phase reconstruction can lead to subcellular imaging without the need for staining. Furthermore, one could also envision the possibility of phase-influencing staining.

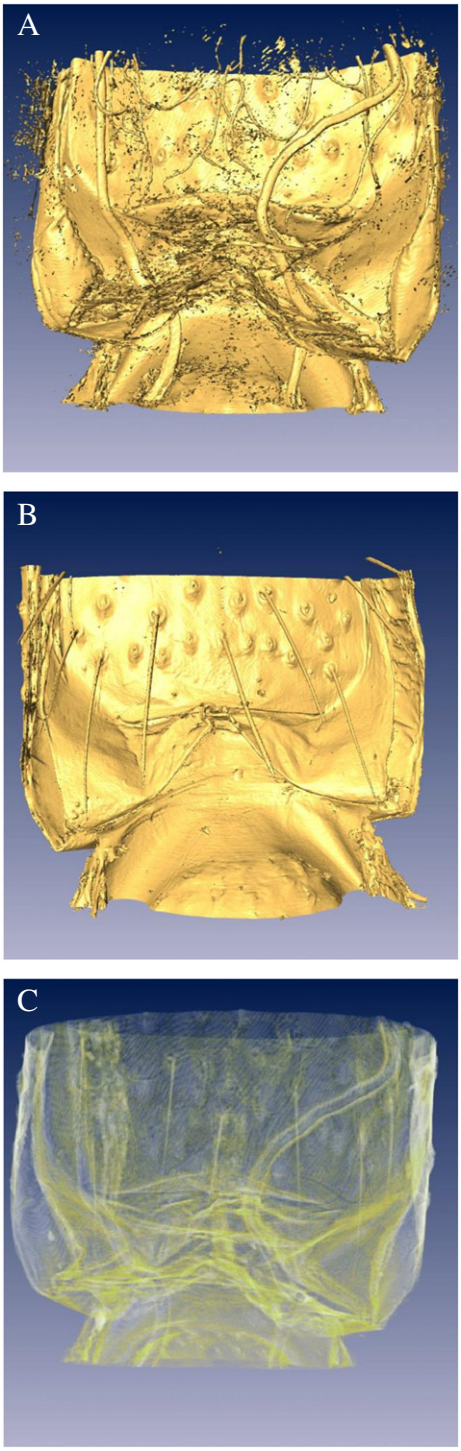

Fig. 13. Tomographic isosurface representation of the abdomen of a mosquito. A: a see-through-view of the abdomen; B: same as (A) but with the front surface removed by image processing: the image reveals fine vessels of a few μm diameter. C: volume rendered representation of the same specimen (see also movie SI13 in Supplementary Data). The width of the mosquito abdomen is ≈400 μm.

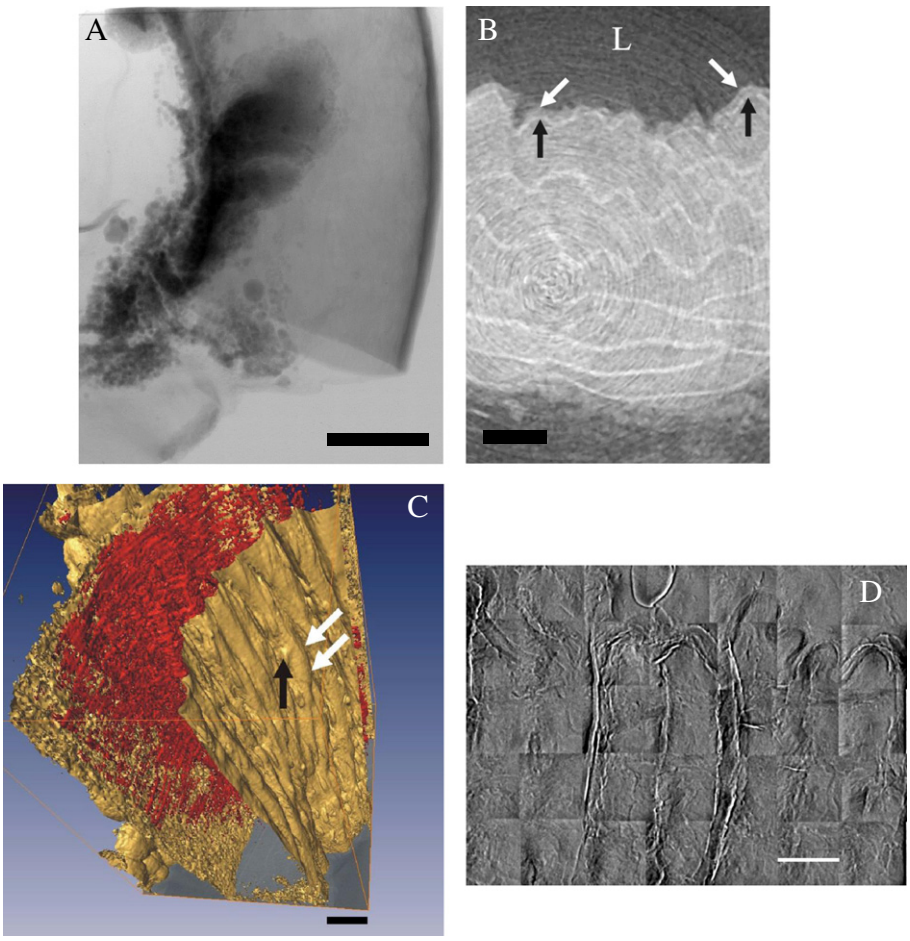

Fig. 14. A: hard-X-ray micrographs of a mouse aorta specimen fixed in resin; the overall specimen dimension, including the resin, was ~5×7×10 mm^3. Bar: 1 mm. B: a tomographically reconstructed slice. Bar = 50 μm. The detailed structure of the vessel wall is clearly seen even if the specimen is larger than the imaged area. C: tomographic volume rendered structure of the same aorta specimen; scale bar: 50 μm. D: ultrahigh resolution radiography of a thinned (200 μm) specimen showing the vessel wall of the mouse aorta. Bar: 20 μm.

3.6. Thick specimens

The key advantage of hard-X-ray microscopy is of course its capability to nondestructively examine thick specimens without complicated preparation procedures. The combination of high penetration and spatial resolution practically results in extreme volume sensitivity. We would like to elaborate here on this point based on a series of practical tests — dealing in particular with the possible impact of the specimen thickness on the spatial resolution.

First of all, good resolution is indeed possible with thick specimens. Fig. 12 shows for example a zebra fish specimen stained using the Golgi method. In Fig. 12A, the black spots indicate individual cells stained by silver dichromate precipitate. Therefore, the spatial resolution is suitable for the identification of cell positions within a thick tissue. Fig. 12B (see also movie SI12B in Supplementary Data) shows the tomographic reconstruction of the zebra fish head. The size of each bright spot is about 5 μm, corresponding to the cell size *in vivo*.

Fig. 13 shows another good example illustrating high volume sensitivity: fine vessels with a diameter of a few microns are clearly observed in the ≈400 μm abdomen of a mosquito (see also movie SI13 in Supplementary Data). With a spatial resolution better than 1 μm and a penetration depth >1 mm, the volume selectivity is then better than 1 part in 10^9.

Such selectivity levels strongly reduce the difficulties in preparing the specimen and in finding the regions of interest for specific studies. The specimens can thus be kept in a rather natural environment. On the contrary, microscopy techniques that can only probe very thin specimens require sectioning (with possible information loss) to reveal 3D structures.

With suitable fixation procedures, we could even obtain high-resolution 3D tomographically reconstructed images of mammalian cells in thick specimens — as shown in Fig. 14 for a portion of mouse aorta fixed in resin. Fig. 14A is one of the raw images used for tomography reconstruction; the overall specimen dimensions (including resin) is ~5×7×10 mm^3. Fig. 14B shows a tomographically reconstructed cross section with a FOV of 240 μm. Note that the detailed wall structure is clearly visible even if the specimen was larger than the imaged area. The aorta wall is covered by the waving elastic laminae, the innermost of which – the internal elastic lamina (black arrows) – is isolated from the lumen (L) by a monolayer of endothelial cells (white arrows).

Fig. 14C presents the volume rendered structure of this specimen. The white arrows indicate the borders between neighboring cells, whereas a black arrow emphasizes a nucleus sticking out from the surface whose outline is well preserved in the reconstruction. Therefore, imaging in these tests goes beyond the mere outline of cells and reveals once again sub-cellular details.

As to the effects of the specimen thickness on the resolution, we find that when using the zone-plate magnifier the best 30 nm Rayleigh resolution level can only be obtained for specimens less than 200 μm thick. This is mainly due to the use of objectives: for TXM with multi-keV photon and high numerical aperture objectives (NA>2×10^{-3}), the depth of focus is of the order of few tens of

μm. For specimen thicker than the depth of focus the resolution worsens. Other factors can negatively affect the resolution, such as strongly scattering materials. Fig. 14D shows for example a high-resolution image of the sliced tissue of a mouse aorta: as the specimen was thinned to 200 μm, the resolution is largely preserved and the wavy structure as well as other fine details can be clearly observed.

High resolution radiographs such as those of Fig. 14 clearly indicate that with appropriate staining full 3D images of sub-cellular organelles can be obtained without a significant decrease in resolution with respect to the raw images. The 3D rendition actually improves the visibility of these tiny structures. The advantage of working with thick specimens is obvious: we can first identify tumor areas and then perform a quantitative analysis of the corresponding Au distribution.

Excessive larger thickness values, however, negatively impact the resolution even in the case of white beam imaging where no concern of objective and depth of focus apply. We empirically found that a resolution suitable for subcellular detection is possible for specimens up to a few mm thick. Larger thickness values lead instead to significant blurring due to scattering — so that for example local tomography reconstruction (Anastasio et al., 2003; Faridani et al., 1997) becomes problematic.

4. Discussion and conclusion

Our experiments demonstrate that microradiology with deeply-penetrating hard-X-rays can now investigate not only individual cells in tissues but also subcellular structures. When spatial resolution is the primary objective, images can be obtained down to the 30 nm Rayleigh resolution level.

The control of different parameters can match the needs of each specific investigation with a compromise between time resolution and spatial resolution. For example, real-time studies conducted with unmonochromatized X-rays and no zone plate magnification combine an excellent time resolution suitable for live specimens with an acceptable spatial resolution (<1 μm).

Our results generally indicate that with its new performance levels X-ray microradiology can significantly expand its role in biological and biomedical investigation. In order to properly appreciate this point, we would like to present a realistic comparison with other microscopy techniques. The general conclusion is that hard-X-ray microscopy does offer marked advantages although, in the end, the best strategy is always a combination of complementary techniques.

Compared to diffraction-limited optical microscopy, our experiments reach a better spatial resolution (<30 nm). Furthermore, the specimen preparation procedures are typically simpler and, most importantly, hard-X-rays can probe thick opaque specimens.

Electron microscopy also requires more complicated and invasive specimen preparation steps. In particular, TEM provides better resolution, but the process of dehydration, embedding and preparing ultra thin sections is complicated and time-consuming. Moreover, TEM can only probe very thin specimens (typically <1 μm) and its contrast is limited. Sample stages with reasonably large tilting angles can be helpful in collecting enough images for tomography reconstruction — limited, however, to thin or small samples. Three-dimensional images of thick samples can be obtained with TEM by serial sections and algorithm reconstruction, but the z-axis resolution is limited.

Our hard-X-ray microscopy can probe thicker specimens (>300 μm in general and up to 10 mm without the magnifying zone plate) than soft X-ray microscopy (<10 μm) and TEM. This makes it possible to examine entire cells, multi-cellular structures or tissues without serial sectioning, eliminating the consequent possibility of losing or distorting information.

The importance of the enhanced role of hard-X-rays in biological and biomedical studies is quite evident. Not only the experimental methods discussed here are complementary to other microscopy techniques, but they could in some cases replace them — for example, TEM in the study of tissues. The role of hard-X-rays microscopy is likely to further expand in the future: additional improvements are indeed possible that would enhance the theoretical and practical performances of the present instruments. We note, for example, the continuous improvements in zone plate technology that brought the resolution to the 20 nm level and is moving towards 15 nm.

Supplementary data to this article can be found online at http://dx.doi.org/10.1016/j.biotechadv.2012.04.005.

Acknowledgments

This work was supported by the National Science and Technology Program for Nanoscience and Nanotechnology, by the Academia Sinica, by Mackay Memorial Hospital (MMH-E-94003) (Taiwan), by the MOST (KOSEF) through National Core Research Center for Systems Bio-Dynamics (Korea), by the Fonds National Suisse de la Recherche Scientifique, and by the Ecole Polytechnique Fédérale de Lausanne. We thank Y. F. Song of NSRRC for the help in the NanoXCT studies.

References

Allen LJ, McBride W, O'Leary NL, Oxley MP. Exit wave reconstruction at atomic resolution. Ultramicroscopy 2004a;100:91-104.
Allen LJ, McBride W, Oxley MP. Exit wave reconstruction using soft X-rays. Opt Commun 2004b;233:77–82.
Anastasio MA, Carlo FD, Pan X. Phase-contrast tomography and the local tomography problem. Proc SPIE 2003;5030:120–6.
Bachim BL, Gaylord TK. Polarization-dependent loss and birefringence in long-period fiber gratings. Appl Opt 2003;42:6816–23.
Baik S, Kim HS, Jeong MH, Lee CS, Je JH, Hwu Y, et al. International consortium on phase contrast imaging and radiology beamline at the Pohang Light Source. Rev Sci Instrum 2004;75:4355–8.
Barty A, Nugent KA, Paganin D, Roberts A. Quantitative optical phase microscopy. Opt Lett 1998;23:817–9.
Barty A, Nugent KA, Roberts A, Paganin D. Quantitative phase tomography. Opt Commun 2000;175:329–36.
Bech M, Bunk O, David C, Kraft P, Brönnimann C, Eikenberry EF, et al. X-ray imaging with the PILATUS 100k detector. Appl Radiat Isot 2008;66:474–8.
Blackburn JP, Peters NS, Yeh HI, Rothery S, Green CR, Severs NJ. Upregulation of connexin43 gap junctions during early stages of human coronary atherosclerosis. Arterioscler Thromb Vasc Biol 1995;15:1219–28.
Chen YT, Lo TN, Chiu CW, Wang JY, Wang CL, Liu CJ, et al. Fabrication of high-aspect-ratio Fresnel zone plates by e-beam lithography and electroplating. J Synchrotron Radiat 2008a;15:170–5.
Chen YT, Lo TN, Chu YS, Yi J, Liu CJ, Wang JY, et al. Full-field hard X-ray microscopy below 30 nm: a challenging nanofabrication achievement. Nanotechnology 2008b;19.
Chen TY, Chen YT, Wang CL, Kempson IM, Lee WK, Chu YS, et al. Full-field microimaging with 8 keV X-rays achieves a spatial resolutions better than 20 nm. Opt Express 2011a;19:19919–24.
Chen YT, Chen TY, Yi JM, Chu YS, Lee WK, Wang CL, et al. Hard X-ray Zernike microscopy reaches 30 nm resolution. Opt Lett 2011b;3:1269–71.
Chen YT, Chen TY, Yi JM, Chu YS, Lee WK, Wang CL, et al. Hard X-ray Zernike microscopy reaches 30 nm resolution. Opt Lett 2011c;36:1269–71.
Chien CC, Wang CH, Wang CL, Li ER, Lee KH, Hwu Y, et al. Synchrotron microangiography studies of angiogenesis in mice with microemulsions and gold nanoparticles. Anal Bioanal Chem 2010;397:2109–16.
Chu YS, Yi JM, De Carlo F, Shen Q, Lee WK, Wu HJ, et al. Hard-X-ray microscopy with Fresnel zone plates reaches 40 nm Rayleigh resolution. Appl Phys Lett 2008;92.
Cloetens P, Ludwig W, Boller E, Helfen L, Salvo L, Mache R, et al. Quantitative phase contrast tomography using coherent synchrotron radiation. Proc SPIE 2002;4503:82–91.
Faridani A, Finch DV, Ritman EL, Smith KT. Local tomography II. SIAM J Appl Math 1997;57:1095–127.
Fischer RS, Wu Y, Kanchanawong P, Shroff H, Waterman CM. Microscopy in 3D: a biologist's toolbox. Trends Cell Biol 2011;21:682–91.
Hsieh W-K, Chen F-R, Kai J-J, Kirkland AI. Resolution extension and exit wave reconstruction in complex HREM. Ultramicroscopy 2004;98:99-114.
Hwu Y, Tsai WL, Groso A, Margaritondo G, Je JH. Coherence-enhanced synchrotron radiology: simple theory and practical applications. J Phys D: Appl Phys 2002;35:R105–20.
Hwu Y, Tsai WL, Chang HM, Yeh HI, Hsu PC, Yang YC, et al. Imaging cells and tissues with refractive index radiology. Biophys J 2004;87:4180–7.

Jacobsen C, Beetz T, Feser M, Osanna A, Stein A, Wirick S. Spectromicroscopy of biological and environmental systems at Stony Brook. Surf Rev Lett 2002;9: 185–91.
Jiang H, Song C, Chen CC, Xu R, Raines KS, Fahimian BP, et al. Quantitative 3D imaging of whole, unstained cells by using X-ray diffraction microscopy. Proc Natl Acad Sci U S A 2010;107:11234–9.
Kirz J, Ade H, Anderson E, Buckley C, Chapman H, Howells M, et al. New results in soft X-ray microscopy. Nucl Instrum Methods B 1994;87:92–7.
Lai SF, Chen WC, Wang CL, Chen HH, Chen ST, Chien CC, et al. One-pot tuning of au nucleation and growth: from nanoclusters to nanoparticles. Langmuir 2011;27: 8424–9.
Larabell CA, Nugent KA. Imaging cellular architecture with X-rays. Curr Opin Struct Biol 2010;20:623–31.
Liu CJ, Wang CH, Chien CC, Yang TY, Chen ST, Leng WH, et al. Enhanced X-ray irradiation-induced cancer cell damage by gold nanoparticles treated by a new synthesis method of polyethylene glycol modification. Nanotechnology 2008;19.
Liu CJ, Wang CH, Chen ST, Chen HH, Leng WH, Chien CC, et al. Enhancement of cell radiation sensitivity by pegylated gold nanoparticles. Phys Med Biol 2010;55: 931–45.
Lo TN, Chen YT, Chiu CW, Liu CJ, Wu SR, Lin IK, et al. E-beam lithography and electrodeposition fabrication of thick nanostructured devices. J Phys D: Appl Phys 2007a;40:3172–6.
Lo TN, Chen YT, Liu CJ, Chang WD, Lai TY, Wu HJ, et al. Using e-beam and X-ray lithography techniques to fabricate zone plates for hard X-ray. In: Choi JY, Rah S, editors. Synchrotron Radiation Instrumentation; 2007b. p. 1466–9. Pts 1 and 2.
Margaritondo G. Elements of synchrotron light: for biology, chemistry, and medical research. Oxford University Press; 2002.
Marsh MN, Peters TJ, Brown AC. Observations of isolated enterocytes and of their subcellular components using transmission and scanning electron microscopy. Gut 1971;12:499–508.
Marton L. The electron microscope: a new tool for bacteriological research. J Bacteriol 1941;41:397–413.
McDermott G, Le Gros MA, Knoechel CG, Uchida M, Larabell CA. Soft X-ray tomography and cryogenic light microscopy: the cool combination in cellular imaging. Trends Cell Biol 2009;19:587–95.
Meyer-Ilse W, Hamamoto D, Nair A, Lelievre SA, Denbeaux G, Johnson L, et al. High resolution protein localization using soft X-ray microscopy. J Microsc 2001;201: 395–403.
Paganin D, Nugent KA. Noninterferometric phase imaging with partially coherent light. Phys Rev Lett 1998;80:2586–9.
Porter KR, Claude A, Fullam EF. A study of tissue culture cells by electron microscopy methods and preliminary observations. J Exp Med 1945;81:233–46.
Rittweger E, Han KY, Irvine SE, Eggeling C, Hell SW. STED microscopy reveals crystal colour centres with nanometric resolution. Nat Photonics 2009;3:144–7.
Shen Q, Lee WK, Fezzaa K, Chu YS, De Carlo F, Jemian P, et al. Dedicated full-field X-ray imaging beamline at advanced photon source. Nucl Instrum Methods A 2007;582: 77–80.
Song YF, Chang CH, Liu CY, Chang SH, Jeng U, Lai YH, et al. Performance of X-ray beamlines at superconducting wavelength shifter. In: Choi JY, Rah S, editors. Synchrotron radiation instrumentation; 2007. p. 808–11. Pts 1 and 2.
Tanaka K, Fukudome H. Three-dimensional organization of the Golgi complex observed by scanning electron microscopy. J Electron Microsc Tech 1991;17:15–23.
Wang CH, Chien CC, Yu YL, Liu CJ, Lee CF, Chen CH, et al. Structural properties of 'naked' gold nanoparticles formed by synchrotron X-ray irradiation. J Synchrotron Radiat 2007;14:477–82.
Wang CH, Liu CJ, Wang CL, Hua TE, Obliosca JM, Le KH, et al. Optimizing the size and surface properties of polyethylene glycol (PEG)-gold nanoparticles by intense X-ray irradiation. J Phys D: Appl Phys 2008;41.
Wang W, Li G, Chen C, Xie S, Zhuang X. Chromosome organization by a nucleoid-associated protein in live bacteria. Science 2011a;333:1445–9.
Wang CH, Liu CJ, Chien CC, Chen HT, Hua TE, Leng WH, et al. X-ray synthesized PEGylated (polyethylene glycol coated) gold nanoparticles in mice strongly accumulate in tumors. Mater Chem Phys 2011b;126:352–6.
Yeh HI, Lu CS, Wu YJ, Chen CC, Hong RC, Ko YS, et al. Reduced expression of endothelial connexin37 and connexin40 in hyperlipidemic mice: recovery of connexin37 after 7-day simvastatin treatment. Arterioscler Thromb Vasc Biol 2003;23:1391–7.
Yi J, Chu YS, Chen YT, Chen TY, Hwu Y, Margaritondo G. High-resolution hard-X-ray microscopy using second-order zone-plate diffraction. J Phys D: Appl Phys 2011;44.
Yin G-C, Chen F-R, Hwu Y, Shieh H-PD, Liang KS. Quantitative phase retrieval in transmission hard X-ray microscope. Appl Phys Lett 2007;90. 181118-181113.
Yun W, Lai B, Krasnoperova AA, Di Fabrizio E, Cai Z, Cerrina F, et al. Development of zone plates with a blazed profile for hard X-ray applications. Rev Sci Instrum 1999;70:3537–41.